

HIGH SPEED VIDEO IMAGING OF OVERHANG SURFACES IN BEAM SHAPED LASER POWDER BED FUSION OF 316L STAINLESS STEEL

L. Vanmunster^{a,b}, A. Dejans^a, B. Van Hooreweder^a, B. Vrancken^{a,b}

a) KU Leuven, Department of Mechanical Engineering, Celestijnenlaan 300, 3001 Leuven

b) FlandersMake@KU Leuven

Abstract

Beam shaping has seen rising interest in the AM industry and research field because of the increased level of control over the spatial distribution of the thermal input during Laser Powder Bed Fusion, allowing for faster build rates. This report investigates if the more uniform heat input offers benefits to the scanning of unsupported overhanging structures. In-situ high speed video imaging is combined with post process surface characterization to derive a relation between the scan parameters and quality of the overhang surface. The best results were achieved at low energy densities, but no clear advantage of top-hat shaped laser spots over the standard Gaussian beams is observed.

Keywords: High Speed Video, Beam shaping, Overhang, Laser Powder Bed Fusion

Introduction

Laser Powder Bed Fusion (LPBF) is a metal Additive Manufacturing process capable of producing highly intricate parts by translating a computer 3D model into layers, which are consequently selectively molten by a high power laser on a fine metal powder bed. By designing the optics train to produce small laser spot sizes, small melt pools and hence small minimal feature sizes are obtainable. However, the small laser spot and thin metal layer thickness, required for good part accuracy and surface quality, severely limit the maximum process speed. One of the mitigation strategies under investigation for this issue is the use of larger spot sizes combined with higher laser powers. However, a mere defocusing of a standard single-mode (Gaussian) laser spot leads to a quickly deterioration beam quality and hence less reliable part qualities [1]. Therefore, different beam profiles with a more uniform heat input are under investigation. These are amongst others Top-hat shaped, Bessel beam shaped or Ring shaped, allowing to achieve consistent temperature distributions across a wider area and reduced temperature gradients [2].

Literature suggests the ring-shaped spots lead to shallower, wider and more stable melt pools [3]. The increased width could lead to a larger process window and hence a significant productivity increase through the use of higher scan speeds and larger hatch distances [4], [5]. However, the larger spot sizes inherently expand the minimal achievable feature sizes. Hence, OEMs try to include multiple beam sizes in a single system, e.g. through the use of multiple scanners or with variable focusing units. Another option is to install a laser with integrated beam shape switching, such as the AFX-1000 laser by nLight inc. [6] which allows switching between a small single-mode shape and a larger multimode ring-shape in between individual scan tracks.

While the different beam shapes are mostly under investigation for their potential gains in productivity, they can also be beneficial to other part qualities. The more uniform energy input might allow for enhanced properties of the overhanging and downfacing areas that are currently a major challenge for conventional beam shapes. In these regions, the laser scans over areas of loose powder without any bulk metal support. The highly reduced thermal conductivity of powder compared to dense metal severely limits the ability of the material to spread the input energy. This results in larger melt pools and increased temperatures, which in turn lead to higher residual stresses and the formation of dross [7]. The latter is a sinking of the melt pool of overhang layers in the powder bed under the influence of capillary forces and gravity and results in a loss of dimensional accuracy [8]. Secondly, the layers exhibit a high level of internal stresses, which can lead to upwards warping and consequent recoating issues. Typically, this is accounted for by adding support structures underneath overhanging areas, to act as a mechanical anchor and heat dissipator. However, the scanning of support structures increases the build time, leads to material waste and increases the postprocessing time, since they have to be removed after production

[9]. Another strategy was investigated by Kruth et al., who implemented feedback control to achieve reduced cross levels [10]. Ashby et al. [11] combined high speed optical imaging with infrared (IR) imaging and simulations to better understand the effect of varying scan parameters on the overhang quality. Their work concluded that a strategy for reduced energy input in the overhanging area is required to prevent material aggregation due to overheating.

This work investigates the potential of a beam shaped laser to improve the dimensional accuracy of overhanging areas in LPBF parts. Post-process surface quality analysis will be combined with in-situ high speed optical imaging to study the physics behind powder agglomeration, cross formation and layer warping.

Methods & Materials

Sample Design

The overhanging areas were studied using bridge-like structures supported on two sides. The overhang samples consist of a 0.5 mm thick bridge build on top of two substrate pillars. All dimensions are displayed in Figure 1.

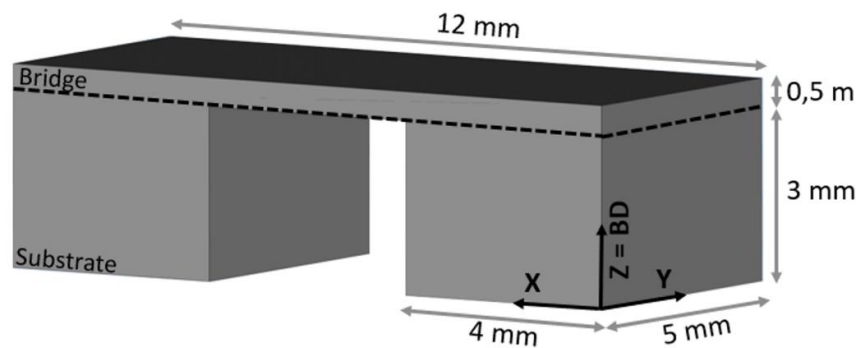


Figure 1: Design and dimensions of the bridge samples. The build direction BD is oriented along the Z axis, while X is the coater direction.

Laser Powder Bed Fusion

All samples were produced on a heavily modified Concept Laser M1 machine that was retrofitted with a AFX-1000 Variable Beam Profile laser from nLight inc. This laser allows for fast switching between multiple beam profiles by dividing the laser power between the single-mode core and multimode-enabling fiber cladding, resulting in a combination of a Gaussian and a ring profile. Seven discrete levels of power distribution between the Gaussian peak and surrounding ring are possible, ranging from index 0 (near 100% single-mode or Gaussian beam) to index 6 (90% of power in the ring). It has a maximum power rating of 600 W in the Gaussian peak and 1200 W in the ring and a 1070 nm wavelength. To accommodate beam switching, the laser and scanner control was transferred to an in-house developed control system, allowing for in-layer beam shape switching. A large aperture Scanlabs scanner and a f-theta lens with focal distance of 420 mm were implemented in the optics train. Due to a defocusing issue in the setup, the Ring shape was not achieved, but rather a 250 μm top-hat shape for index 6 was measured, while the Gaussian-shaped index 0 spot was measured to be 150 μm wide. All samples were built using 316L stainless steel powder from Höganäs (Sweden) with a 15 to 45 μm particle size range, under an Argon atmosphere (gas flow in the Y direction of Figure 1). To reduce the likelihood of a warped sample damaging the recoater, all samples were oriented with their long axis in the recoater direction (X axis in Figure 1). A zigzag (meander) scan strategy without contours was used, where the hatching orientation is altered by 90° for every subsequent layer. By using a fixed layer thickness set to 30 μm , a total of 17 overhanging layers were scanned. The first overhang scan is oriented in the X direction (see Figure 1), perpendicular to the substrate pillar edge as this is thought to be preferential for part quality [10].

In-situ high speed optical imaging

For high speed optical observations, a Phantom VEO 640 high speed video camera was used, combined with an Infinity Model K2 DistaMax long range microscope lens. Videos were captured at a frame rate of 18000 Hz with a 53.8 μs exposure time and a resolution of 512x384 pixel. During recording, an LED lighting system of approximately 50000 lux was focused on the recorded area. Although the camera and lens were positioned outside

of the Concept Laser M1 machine, a mirror set up in the build chamber ensured a viewing angle perpendicular to the build plate. The overall setup resulted in a field of view of approximately $5.2 \times 3.9 \text{ mm}^2$, equivalent to a pixel size of just over $10 \times 10 \text{ }\mu\text{m}^2$.

Post-situ surface characterization

For imaging of the overhang surface after production, as well as for the cross depth measurements, a Keyence VHX-6000 Digital Microscope was used. By applying a 100x magnification, a 3D image of a $3.5 \times 2.5 \text{ mm}^2$ surface in the center of the overhang area is measured using a Depth of Focus method. An in-house developed Matlab code was used for the image processing, such as creating an average profile along the scan direction.

Results & Discussion

Dimensional accuracy of overhang region

To examine the effect of varying the laser power P , scan speed v and hatch spacing h , as well as the spot shape and size, 100 bridges were built with varying parameter combinations. Figure 2 gives an overview of the parameter ranges examined. Only the index 0 and index 6 beam shapes were used, and will be referred to as ‘Gauss’ and ‘Top-hat’, respectively. All samples used equal parameters for the substrate pillars ($P = 285 \text{ W} - v = 800 \text{ mm/s} - h = 95 \text{ }\mu\text{m}$ – Gaussian shape), only varying parameters in the 17 overhanging layers.

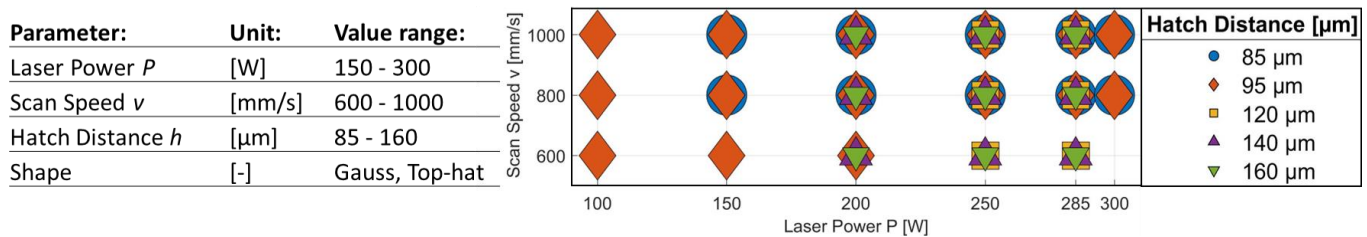


Figure 2: Overview of the investigated parameter ranges. Every combination of P , v & h was built once with index 0 (Gauss shape) and once index 6 (top-hat shape).

For every bridge, the resulting height of the overhanging area was measured by averaging 30 measurements of the height difference between the center of the bridge’s downfacing surface and the top surface, as schematically presented in Figure 3a. The resulting height measurements are shown in Figure 3b relative to the Volumetric Energy Density (VED) of the overhang parameters, which is calculated as:

$$VED = \frac{P}{v \cdot \frac{h}{1000} \cdot \frac{t}{1000}} \left[\frac{\text{J}}{\text{mm}^3} \right] \quad (1)$$

With P the laser power [W], v the scan speed [mm/s], h the hatch spacing [μm] and t the layer thickness [μm].

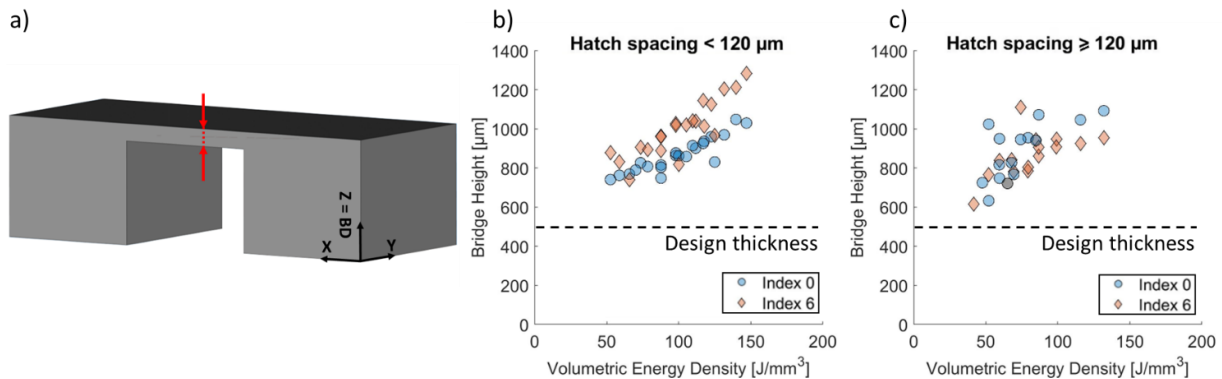


Figure 3: Measurement of bridge height: a) example of the measurement location; b) resulting measured bridge heights for samples with small hatch spacing, where the design thickness was $500 \text{ }\mu\text{m}$; c) resulting measured heights for sample with large hatch spacing, where the design thickness was $500 \text{ }\mu\text{m}$. Samples that did not have a flat top surface were not included in the figure.

Not all parameters lead to defect free parts. Generally, two types of failure are observed. Firstly, when the input energy density is lower than 50 J/mm^3 , insufficient melting occurs to achieve a solid top layer. Secondly, most failures occur due to a full or partial separation in the bridging surface layer. This warping effect is generally attributed to internal stresses in the layer as a result of rapid and uneven heating/cooling cycles. This upwards curling of the surface prevents proper application of the following powder layer, which further hinders the development of a solid top layer.

The measurement results are summarized in Figure 3, excluding the failed samples. Across all samples, a clear increasing trend between the energy input and bridge height is observed. Since each bridge is composed of the same amount of layers, the variation in bridge height is not related to the CAD design, but to other effects: capillary forces cause dross formation and gravity causes a sinking of the molten material in the powder bed. A decrease in input energy density leads to a decrease in melt pool size, reducing the time the material is in a liquid state, thus hindering capillary workings and hence a decrease in bridge height is observed [7]. This explains the relation between the observed bridge height and energy input. When comparing the effect of the laser shape, two observations are made:

- In the parameter combinations where the hatch spacing was smaller than approximately half the top-hat laser spot size (i.e. $<120 \mu\text{m}$), the Gaussian index 0 beam leads to thinner bridges, even at equivalent energy levels. It appears that, even though the index 6 top-hat shape spreads the energy over a larger area, this increases the time the material is in molten state. Hence the melt beads could grow larger and penetrate deeper in the powder bed. This could be the result of the remelting that occurs in every consecutive melt track, since there is considerable overlap between the tracks of consecutive scan vectors. Figure 4 is an illustration of this remelting, where the orange remelting zone overlaps with the previous scan track.
- When comparing the parameters with larger hatch spacing (i.e. $\geq 120 \mu\text{m}$), there is no discernable difference in behavior between the index 0 and index 6 beams. Overall, the spread on the results is larger in the case of larger hatch spacing, potentially owing to an increased denudation effect. Still, the resulting bridge heights at equal energy densities are lower in the large hatch cases. Presumably the remelting in every step discussed above has a stronger effect on the bridge size than the level of *VED*.

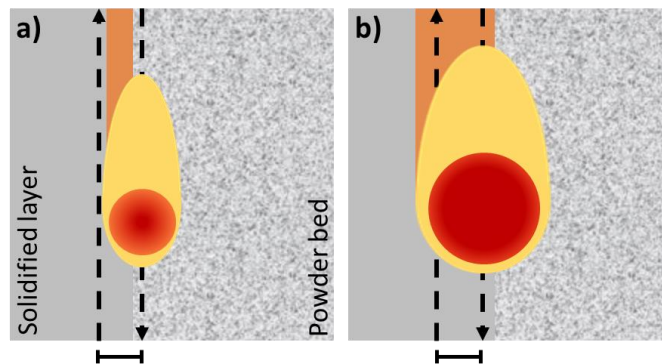


Figure 4: Schematic representation of the remelting due to small hatch spacing and large spot size: a) small Gaussian laser spot with small hatch spacing. The orange remelting zone does not overlap with the previous scan track; b) large top-hat shaped spot with small hatch spacing, exceeding the distance between consecutive tracks. A significant remelting zone is indicated in orange, with clear remelting of the previous track.

High Speed Video Imaging

For some parameter sets, the processing of the first layer of the overhang was recorded using a stationary off-axis high speed imaging system. An example of an image acquired in this way is shown in Figure 5. The goal of these videos is to help visualizing the difference in process behavior in the transition from dense material (i.e. the substrate pillar) to scanning on loose powder (the overhang region). The lower thermal conductivity greatly reduces the process stability, with the videos showing a visible increase in the amount of spatter and denudation. The melt pool is no longer continuous, but rather forms non-connected or loosely connected individual droplets, which is known as balling. This effect is the result of surface tension of the liquid melt pool that can no longer be counteracted by adhesion to a previously solidified layer [12]. This was also partially observed by Ashby et al. [11], albeit in this work at much lower power levels than they used, leading to smaller bead sizes. The overhanging

part of the sample also glows for several hundreds of ms after the passage of the laser, which is again a direct result of the low thermal conductivity of the powder. This effect was measured as the time it took a specific region to reach stable intensity values. While the exact glow time depends on lighting conditions, camera properties and settings, a relative comparison between samples can be made. On average a 192 ± 33 ms afterglow was measured on the high speed videos in the center overhang part, while no visible afterglow is noticeable in the solid substrate. Hence, suggesting the cooling rate in the first overhang layer is orders of magnitude lower compared to the substrate pillar. The afterglow measurements are shown in Figure 6. The afterglow time is found to correlate well with the *VED*, but did not show a statistically significant difference between Gaussian laser and top-hat laser samples at equal scan parameters. The effect of thermal conductivity can also be seen by comparing afterglow measurements in the overhang center (indicated as point C in Figure 5c) to those in the transition between substrate and overhang edge (point E). Point C is located about 2 mm from point E. On average, the transition region E cools down about 45% faster than the overhang center C, likely showing the effect of the substrate pillar as a heat sink. Lastly, the scanned layer visibly sinks in the powder bed during cooldown, thereby aggravating the dimensional deviation of the sample compared to the CAD design.

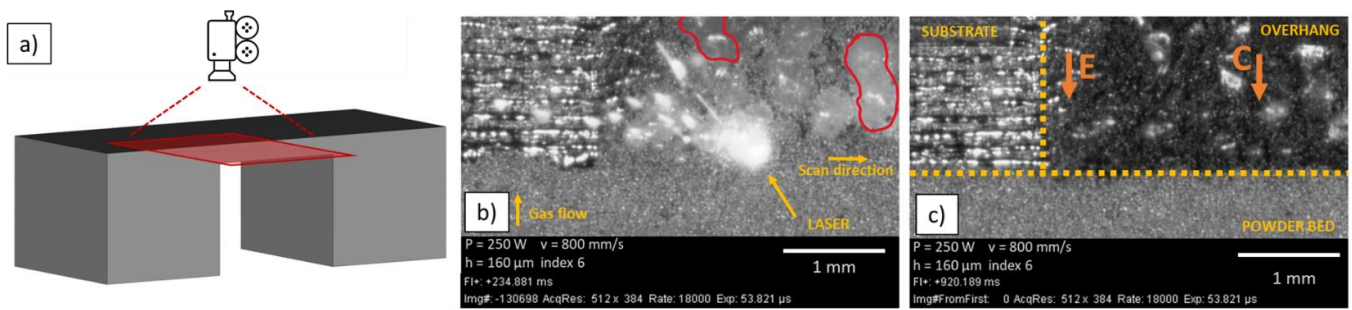


Figure 5: Still frame from the high speed imaging showing the difference in melt quality atop the substrate pillars and overhanging powder layer: a) schematic showing the position of the image in red; b) during the scanning process. Some glowing metal beads are indicated in red, spanning more than 1 scan track in size; c) after scanning and cooldown. Locations of afterglow measurements are indicated by the orange arrows for the overhang center (C) and overhang edge (E).

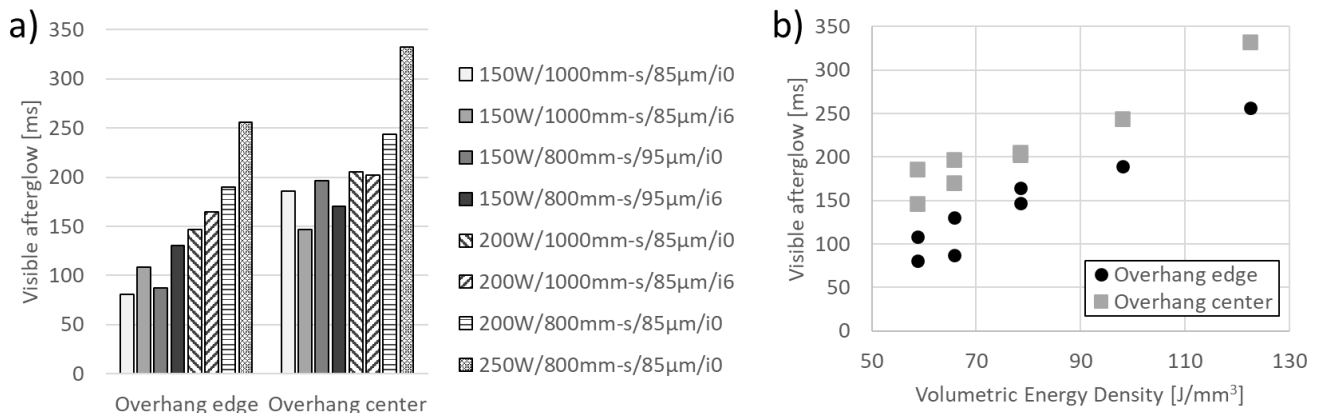


Figure 6: Measurement of visible afterglow due to elevated temperature and low powder thermal conductivity for locations measured on the overhang edge or in the overhang center: a) afterglow measurements per parameter combination. The location of edge and center are indicated in figure 5c by points E and C respectively; b) afterglow compared to energy input.

Figure 7 shows a comparison between the first layer behavior of the index 0 and index 6 laser spots for three different *VED* levels. An increase in energy input leads to increased bead sizes, as is also observable in the boxplots of the bead surface areas on the right side of the figure. This behavior is true for both laser spot shapes under investigation. When comparing index 0 and index 6 first layers at equivalent energy input levels, an increase in average bead surface area is also noticed. This increase is dependent on the energy input level and ranges from +30% to +60% larger bead size when switching from a smaller Gaussian spot to a larger top-hat, while keeping the other scan parameters constant. Hence, the larger spot size presumably allows the material to stay in molten state for a longer time, increasing the probability of larger bead formation. In Figure 7f, the powder bed is still

glowing at the end of the recorded video. Even though the energy levels per mm^2 are similar between figures (e) and (f), the slower scan speeds increase the laser-material interaction time and hence might result in much larger beads. As these image were taken for parameter sets with smaller hatch spacing, the increased bead size could be a cause for the difference in bridge thickness when varying the laser spot shape observed in the previous section.

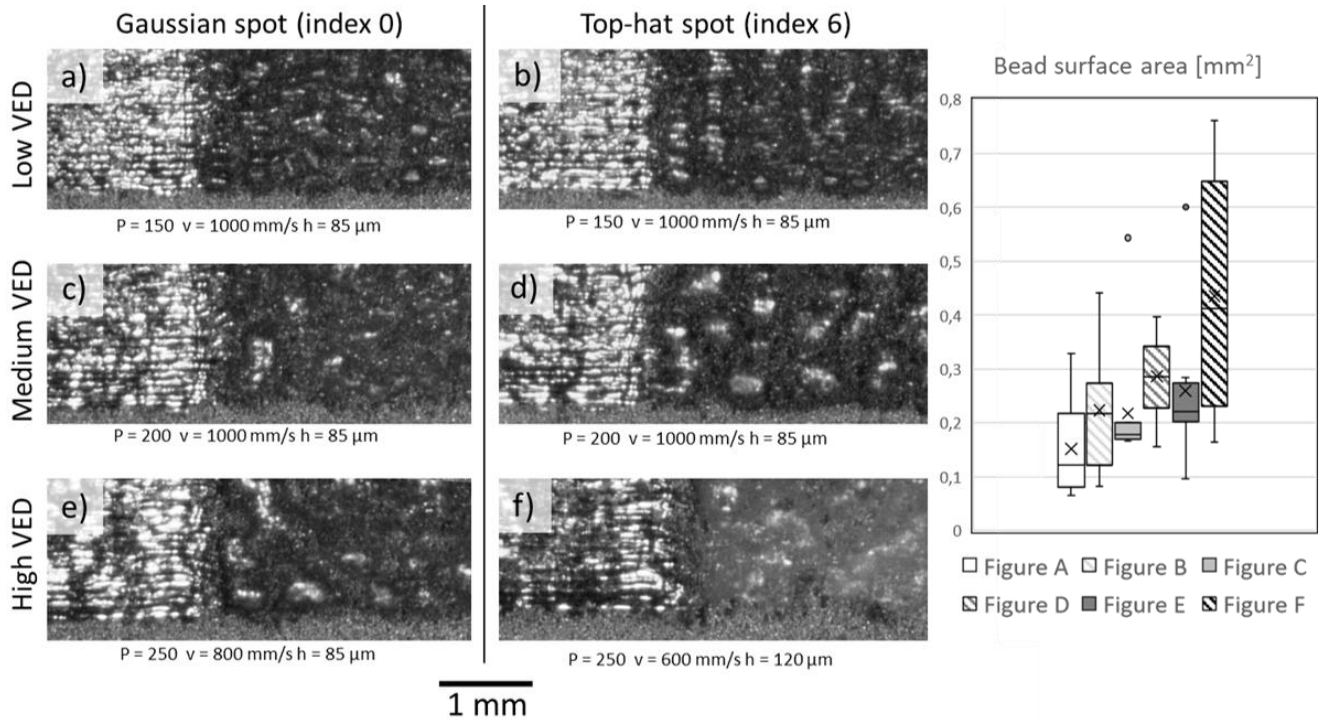


Figure 7: Overview of overhang layers after the first scan, with varying parameter sets. Figure f was still glowing at the end of the recording due to excessive energy input and slow scan speeds. Box plots shows the bead size measurements for each parameter set a – f, with X representing the average bead size.

Interestingly, a certain periodicity develops in the beads on loose powder for some parameter combinations. Subsequent tracks fuse preferentially to the beads formed by the previous scan track, which causes a growth of the beads in the direction perpendicular to the scan vectors. Figure 8 illustrates this behavior. This could result from a combination of the beads acting as a heat sink and adhesion between currently molten and previously solidified material. Since the coalescence of molten beads draws material particles from the surrounding powder bed, the areas in between beads also form a line perpendicular to the scan direction. An example is highlighted in Figure 9a. The effect most likely leads to an increased risk of layer warping. These line-like powder free zones between the beads could act as mechanically weak zones in the layer due to their lack of material. The risk of cracking might be aggravated even further because the weak lines are oriented approximately perpendicular to the direction of largest interior cooling-related stresses [13]. From the videos, it can be observed that the layer breaks along these weak zones during cooling, resulting in individual “islands” of fused material surrounded by cracks. These islands are seen the move independently of each other during cooling. Figure 9 is used to indicate the size of the individual islands that were observed.

For the parameter combination shown in Figure 9, a remelting step was performed approximately five seconds after the first melting scan, to try to fuse the individual solidified islands together. This was only tried for one parameter combination, as an initial estimate for the usefulness of remelting for overhangs. During cooldown, the formation of at least one crack was still visible, as shown in (c), but the amount of cracks is reduced, since the individual islands are fusing together. Conversely, this remelting step also visibly increased the melt bead size and amount of layer sinking in the powder bed. Hence, no further investigation of remelting was performed.

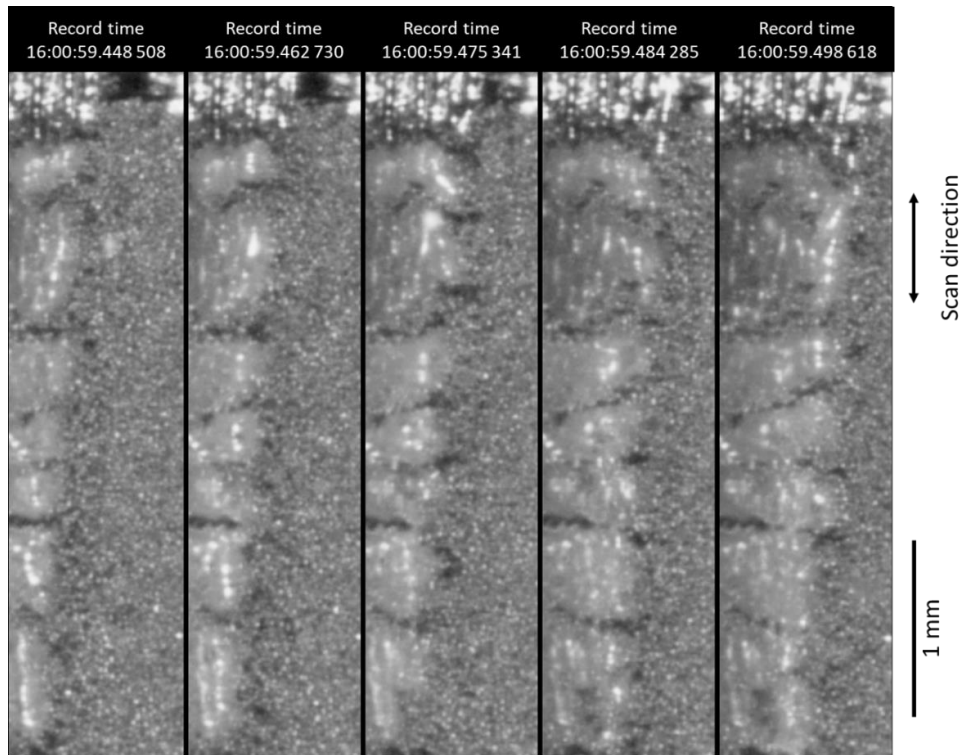


Figure 8: Crack growth due to coalescences of consecutive molten beads. Between every image one extra vector is scanned. The black lines are material lacking zones in between the molten beads, clearly showing growth approximately perpendicular to the scan tracks. Hence, the molten beads also form horizontal lines.

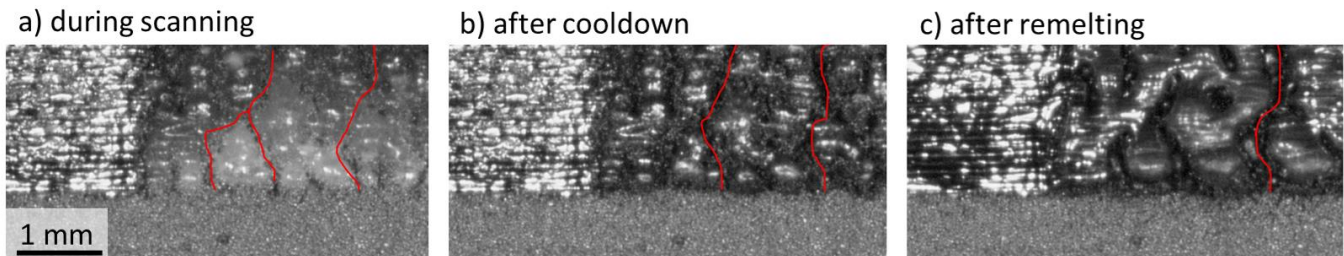


Figure 9: Still frames of parameter combination $P = 150W$, $v = 800\text{mm/s}$, $h = 95\mu\text{m}$, index 0: a) right after melting, the overhang surface still glows and shows the melt beads coalescing, leading to line like weak zones; b) after cooling, 2 cracks formed in the solidified overhang layer. The resulting islands are seen moving independently of each other; c) after remelting and cooling one crack is still present.

Post-process Surface Quality Analysis

To validate the findings from the video analysis, the downfacing surface of the successfully printed parts were optically scanned using a Depth from Defocus method to form a 3D representation of the surface, an example result of which is shown in Figure 10. From these images a height map can be extracted to study the dross beads and intermediate weak zones discussed in previous paragraphs. The level of connectivity of the dross beads could be a good measure for the thermal and mechanical support a layer provides for the next one. The degree of connectivity can be studied by calculating the average profile of the measured surface perpendicular to the scan direction. This is done by summing all data points in the Y direction and normalizing the result, an example of which is shown in Figure 10c. Any continuous material lacking zones show up as sharp valleys in the averaged profile.

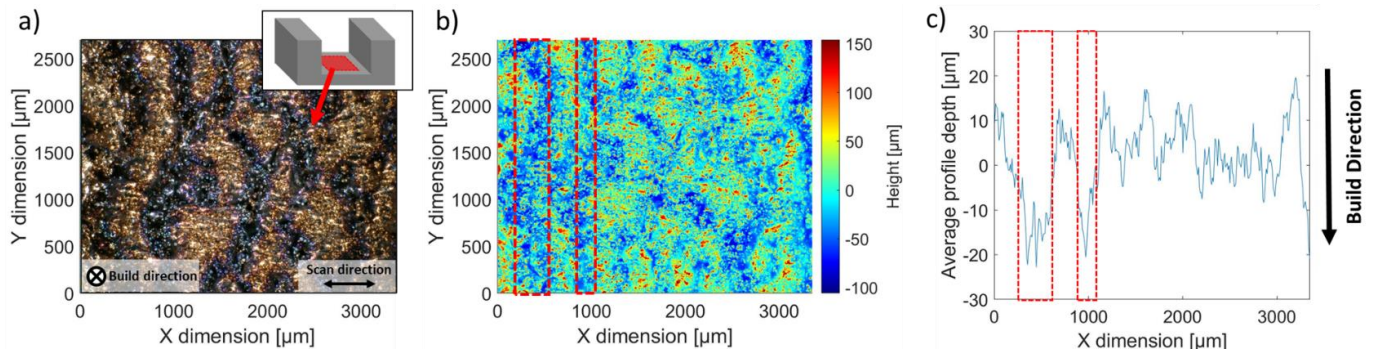


Figure 10: Analysis of the resulting downfacing surface of parameter set [150W, 1000mm/s, 85µm, single-mode]: a) 3D optical image at 100x zoom; b) height map of the 3D image in (a); c) averaged profile along the Y direction. Red lines are used to indicate continuous deep valleys in the 3D surface and averaged profile.

Figure 11 show the height maps and averaged profiles for three parameter sets. The medium-low *VED* level in (a) and (d) shows a low degree of periodicity, leading to a successfully printed sample. Meanwhile, sharp peaks in the averaged profile of the low *VED* sample in (b) and (e) indicates the presence of multiple weakened zones in the top surface, with valley more than twice the layer thickness used. This sample failed due the layer warping and insufficient melting. The sample in (c) and (f) does not show deep weak zones, but the high energy input in this high *VED* sample lead to a significant curvature of the bridge's bottom surface towards the build plate, which indicates sinking of the material in the powder bed.

In order for a layer to fail due to warping, two conditions need to be satisfied. Firstly, there has to be a significant stress level in the sample and secondly the underlying material layer must be too weak to carry this stress. Thus, a bridge should be sufficiently thick and have as few line-like cracks in the surface as possible. Four quality metrics were be examined for a good parameter combination: (1) it should lead to good dimensional accuracy of the bridge height, (2) to a low degree of curvature in the bridge bottom surface, (3) the absence of weaker zones that could cause warping under stress buildup, and finally (4) a fast recuperation to bulk processing quality. Figure 12 gives an overview of these 4 metrics for all samples. Here, the samples are divided in 3 groups based on the quality of the top surface, i.e. how well a parameter set can recuperate to acting as a solid bridge after 0.5 mm of overhanging layers. Good quality parameter combinations lead to flat top surfaces without any remaining signs of the overhanging area. Sufficient quality samples are almost flat, showing a slight curvature in the bridge outer edges, but are most likely recuperating to a fully flat surface if the build job would be continued. Bad quality samples either did not lead to a bridge in one piece or have such a bad quality top surface that further building is not expected to not lead to dense samples.

Figure 12a shows the bridge height compared to *VED*, as already discussed earlier, but also includes the top surface quality grouping. Below 50 J/mm³, no good quality parameter combinations were found, indicating an insufficient energy level for good fusing of material. Conversely, the test did not show good quality bridges above 118 J/mm³, with failures probably linked to high thermally induced stresses as a result of excessive heat input.

In Figure 12b, the deepest material lacking zone for every average profile is plotted. There is no clear link between the energy input level and the depth of these zone. There is however a good correlation between the level of depth and the chance a sample fails to achieve a good quality top surface. No good quality samples were built if a crack deeper than 60 µm (i.e. twice the layer thickness) is present. We can thus use this metric as a measure for how close the sample was to failing due to warping. The only exception is a parameter set with such an excessive bridge height that the crack depth is too small compared to the dross formation and hence thickness of the first layer to cause failure.

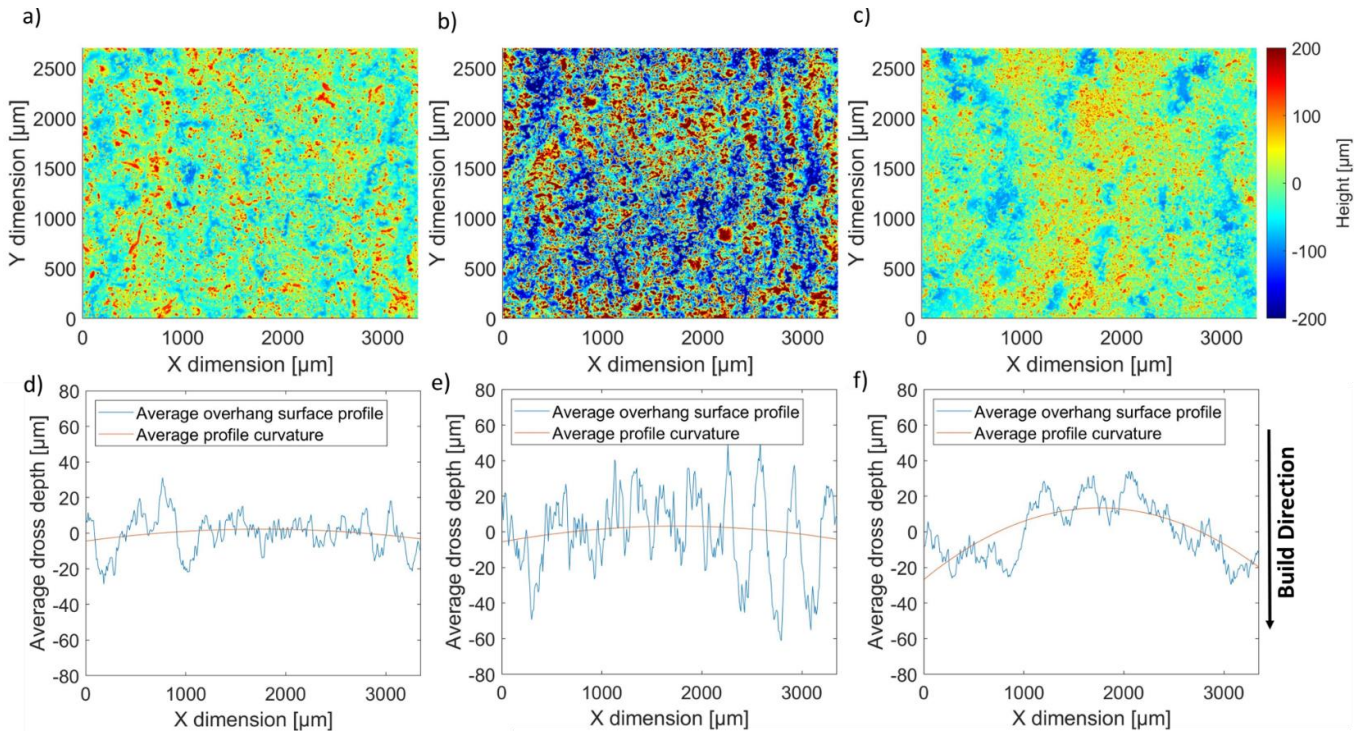


Figure 11: example height maps and averaged profiles for three parameter sets: a/d) medium-low VED parameter (52 J/mm^3) set with no deep valleys and no curvature; b/e) low VED parameter set (35 J/mm^3) with clear onset of cracking; c/f) high VED parameter set (112 J/mm^3) with low valley depths but a high degree of curvature.

Finally, the curvature of the overhang surface is represented in Figure 12c. Here, a negative curvature means the bottom surface of the bridge curves downwards, i.e. towards the build plate. Samples with a high energy input curved downwards, which is linked to a high degree of dross formation, but also to the sinking of the powder bed as shown in the high speed video imaging and was also observed in Figure 11f. The high energy levels and corresponding long interaction time between liquid metal and powder particles directly underneath exaggerate the sinking. This effect opposes the expected upwards curling due to thermal stress. A decrease in energy input induces reduced levels of sinking and hence reduced curvature. At the lowest levels of VED tested, the average curve is directed upwards, indicating that warping forces are greater than the sinking effect.

When an optimized overhanging parameter set needs to be defined, the information in the graphs described above can be combined. The best quality parameters lead to low bridge heights (VED slightly above 50 J/mm^3 in our experiments), low bottom surface profile depths and low curvature values. For the Gaussian beam shape samples, this led to one best set: $P = 150 \text{ W}$, $v = 1000 \text{ mm/s}$ & $h = 95 \text{ }\mu\text{m}$, which is a VED level of 53 J/mm^3 . For the top-hat beam shape samples, two different sets are identified. When optimizing for bridge height this was $P = 285 \text{ W}$, $v = 1000 \text{ mm/s}$ & $h = 120 \text{ }\mu\text{m}$ (79 J/mm^3), while the lowest curvature was achieved at $P = 150 \text{ W}$, $v = 1000 \text{ mm/s}$, $h = 85 \text{ }\mu\text{m}$ (59 J/mm^3). Note that the latter set for index 6 is almost the same parameter set as the optimal index 0 setting. This confirms that, at least in the parameter ranges and optical setup investigated in this report, no noticeable advantage of larger top-hat laser beams compared to small Gaussian beams was found. However, if larger parameter ranges, especially larger hatch spacing are examined, a difference might still arise.

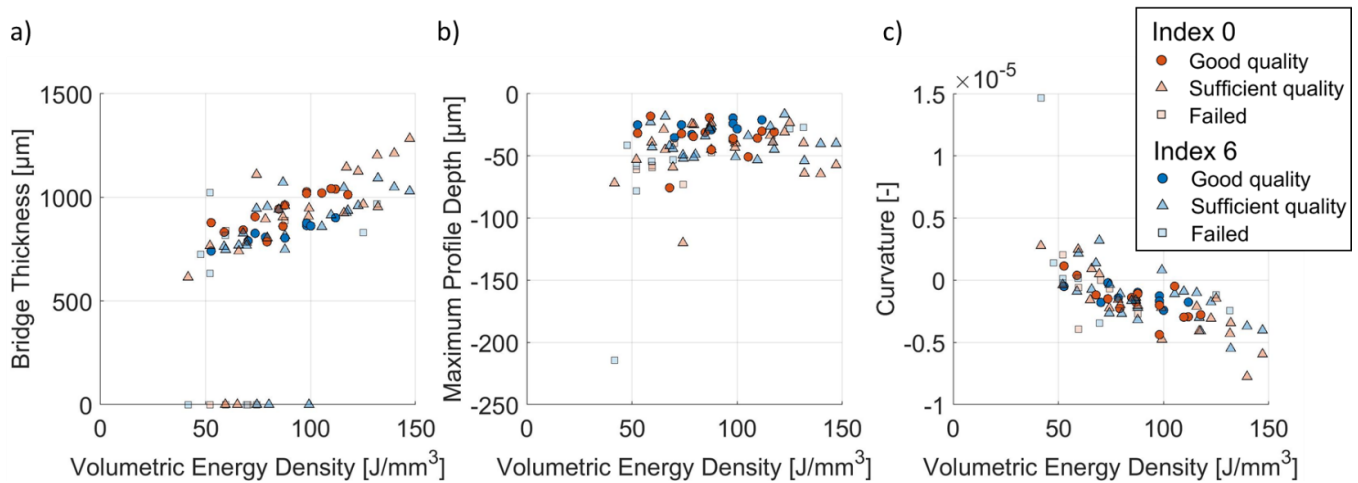


Figure 12: Bridge dimensional quality metrics versus VED: a) Bridge height versus energy density, cfr. in figure 3. Useful energy levels for overhang scans range from 50 – 120 J/mm²; b) Maximum valley depth versus VED. With one exception, all good parts have a valley depth below 60 µm; c) downfacing surface curvature versus VED, showing an inverse relation.

Conclusion

In this report in-situ high speed imaging and post-process surface characterization are used to study the Laser Powder Bed Fusion (LPBF) process in an unsupported overhang situation. The focus lays especially on comparing the effect of a change in spot shape and size on the bridge quality:

- The dimensional accuracy of overhang bridges was measured by characterizing the levels of dross and material sinking with varying laser power, scan speed and hatch spacing. A clear relation between the energy input and depth of material sinking is observed.
- High speed videos showed how the discontinuous melt pool coalesces in the beads perpendicular to the scan track. The first scanned layer was found to not necessarily be a solid layer, but rather a series of individual fused islands surrounded by cracks.
- Optical imaging of the resulting overhang surfaces were used to study the quality metrics of a sufficient overhang part.
- The optimal parameter sets for dimensionally accurate overhangs for Gaussian beam and top-hat beam lasers are almost identical in the investigated parameter range, indicating no immediate benefit of the top-hat shape when the hatch spacing values are similar or lower than its spot size. Enlarging the investigated parameter window might lead to different conclusions and is hence a logical starting point for further studies.

Acknowledgements

The authors acknowledge the funding provided by the Fonds Wetenschappelijk Onderzoek (FWO) of the Flemish government under grant number 1S53722N.

References

- [1] G. Y. Belay *et al.*, “Dynamic optical beam shaping system to generate Gaussian and top-hat laser beams of various sizes with circular and square footprint for Additive Manufacturing applications,” *Procedia CIRP*, vol. 111, pp. 75–80, 2022, doi: 10.1016/j.procir.2022.08.134.
- [2] T. U. Tumkur *et al.*, “Nondiffractive beam shaping for enhanced optothermal control in metal additive manufacturing,” *Sci. Adv.*, vol. 7, no. 38, 2021, doi: 10.1126/sciadv.abg9358.
- [3] T. M. Wischeropp, H. Tarhini, and C. Emmelmann, “Influence of laser beam profile on the selective laser melting process of AlSi10Mg,” *J. Laser Appl.*, vol. 32, no. 2, p. 022059, 2020, doi: 10.2351/7.0000100.
- [4] J. Grünewald, F. Gehringer, M. Schmöllner, and K. Wudy, “Influence of ring-shaped beam profiles on process stability and productivity in laser-based powder bed fusion of AISI 316L,” *Metals (Basel)*, vol. 11, no. 12, pp. 1–18, 2021, doi: 10.3390/met11121989.
- [5] A. Metel, M. Stebulyanin, S. Fedorov, and A. Okunkova, “Power Density Distribution for Laser Additive

- Manufacturing (SLM): Potential, Fundamentals and Advanced Applications,” *Technologies*, vol. 7, no. 1, p. 5, 2018, doi: 10.3390/technologies7010005.
- [6] nLight Inc., “No Title,” *AFX Programmable Fiber Laser - True single-mode to ring-mode beams*, 2022. <https://www.nlight.net/programmable-rackmount-single-mode-fiber-lasers>.
- [7] K. Q. Le, C. H. Wong, K. H. G. Chua, C. Tang, and H. Du, “Discontinuity of overhanging melt track in selective laser melting process,” *Int. J. Heat Mass Transf.*, vol. 162, 2020, doi: 10.1016/j.ijheatmasstransfer.2020.120284.
- [8] P. Lin, M. Wang, V. A. Trofimov, Y. Yang, and C. Song, “Research on the Warping and Dross Formation of an Overhang Structure Manufactured by Laser Powder Bed Fusion,” *Appl. Sci.*, vol. 13, no. 6, p. 3460, 2023, doi: 10.3390/app13063460.
- [9] M. Mele, A. Bergmann, G. Campana, and T. Pilz, “Experimental investigation into the effect of supports and overhangs on accuracy and roughness in laser powder bed fusion,” *Opt. Laser Technol.*, vol. 140, no. November 2020, 2021, doi: 10.1016/j.optlastec.2021.107024.
- [10] P. Mercelis, J. P. Kruth, and J. Van Vaerenbergh, “Feedback control of selective laser melting,” *Proc. 15th Int. Symp. Electromachining, ISEM 2007*, pp. 421–426, 2007.
- [11] A. Ashby *et al.*, “Thermal history and high-speed optical imaging of overhang structures during laser powder bed fusion: A computational and experimental analysis,” *Addit. Manuf.*, vol. 53, p. 102669, 2022, doi: 10.1016/j.addma.2022.102669.
- [12] J. P. Kruth, L. Froyen, J. Van Vaerenbergh, P. Mercelis, M. Rombouts, and B. Lauwers, “Selective laser melting of iron-based powder,” *J. Mater. Process. Technol.*, vol. 149, no. 1–3, pp. 616–622, 2004, doi: 10.1016/j.jmatprotec.2003.11.051.
- [13] T. Simson, A. Emmel, A. Dwars, and J. Böhm, “Residual stress measurements on AISI 316L samples manufactured by selective laser melting,” *Addit. Manuf.*, vol. 17, pp. 183–189, 2017, doi: 10.1016/j.addma.2017.07.007.